Am J Physiol Heart Circ Physiol 297: H208–H222, 2009.
First published May 8, 2009; doi:10.1152/ajpheart.00037.2009.

Validation of a one-dimensional model of the systemic arterial tree

Philippe Reymond,[1] Fabrice Merenda,[1] Fabienne Perren,[2] Daniel Rüfenacht,[3] and Nikos Stergiopulos[1]

[1]*Laboratory of Hemodynamics and Cardiovascular Technology, Ecole Polytechnique Fédérale de Lausanne, Lausanne; and* [2]*Neurology Department of Clinical Neurosciences,* [3]*Neurointerventional, University Hospital and Medical Faculty of Geneva, Geneva, Switzerland*

Submitted 12 January 2009; accepted in final form 4 May 2009

Reymond P, Merenda F, Perren F, Rüfenacht D, Stergiopulos N. Validation of a one-dimensional model of the systemic arterial tree. *Am J Physiol Heart Circ Physiol* 297: H208–H222, 2009. First published May 8, 2009; doi:10.1152/ajpheart.00037.2009.—A distributed model of the human arterial tree including all main systemic arteries coupled to a heart model is developed. The one-dimensional (1-D) form of the momentum and continuity equations is solved numerically to obtain pressures and flows throughout the systemic arterial tree. Intimal shear is modeled using the Witzig-Womersley theory. A nonlinear viscoelastic constitutive law for the arterial wall is considered. The left ventricle is modeled using the varying elastance model. Distal vessels are terminated with three-element windkessels. Coronaries are modeled assuming a systolic flow impediment proportional to ventricular varying elastance. Arterial dimensions were taken from previous 1-D models and were extended to include a detailed description of cerebral vasculature. Elastic properties were taken from the literature. To validate model predictions, noninvasive measurements of pressure and flow were performed in young volunteers. Flow in large arteries was measured with MRI, cerebral flow with ultrasound Doppler, and pressure with tonometry. The resulting 1-D model is the most complete, because it encompasses all major segments of the arterial tree, accounts for ventricular-vascular interaction, and includes an improved description of shear stress and wall viscoelasticity. Model predictions at different arterial locations compared well with measured flow and pressure waves at the same anatomical points, reflecting the agreement in the general characteristics of the "generic 1-D model" and the "average subject" of our volunteer population. The study constitutes a first validation of the complete 1-D model using human pressure and flow data and supports the applicability of the 1-D model in the human circulation.

wave propagation; heart model; cerebral circulation; ventricular-vascular coupling; nonlinear viscoelasticity; ultrasound; noninvasive vascular imaging

ONE-DIMENSIONAL (1-D) MODELS of the arterial tree are, to date, the models of choice for studying pressure and flow wave propagation in the arterial system. The primary reason is that 1-D flow equations are hyperbolic in nature and thus well adapted to describe wave propagation phenomena. Furthermore, the solution is given only for one spatial dimension and time and thus 1-D models do not require high computational power. In contrast, three-dimensional computational fluid dynamics models including fluid-structure interaction, although in principle amenable to describe wave phenomena, are computationally very intense and in consequence more adapted to studying detailed local flow fields rather than pressure and flow waves over extended regions or the entire arterial tree.

Distributed 1-D models of the arterial tree have been used extensively in the past (cf. Table 1 for review) for simulating wave propagation in the entire (2, 13) or parts of the arterial tree (6, 48, 50, 69) under various physiological (44, 50, 55, 70, 74) or pathological conditions (1, 3, 9, 36, 64, 71). Careful examination of the different 1-D models (Table 1) reveals that these models vary substantially in many essential aspects of their formulation. The main differences, categorized in Table 1, pertain to the following: *1*) incorporation, or not, of a heart left ventricular (LV) model, this aspect is essential for studying ventricular-vascular coupling effects; *2*) completeness of the systemic arterial tree, entire systemic circulation or parts thereof; *3*) detailed description of the cerebral and coronary arteries; *4*) inclusion of wall viscoelastic properties; *5*) approximation of wall shear stress; *6*) approximation of the convective acceleration term; and *7*) boundary conditions at terminal sites.

Table 1 shows that out of the 13 previously published 1-D models of the entire systemic circulation, only 2 of them [Formaggia et al. (14) and Fitchett (13)] incorporated a heart model allowing for some degree of ventricular-vascular coupling; all others specified aortic flow or pressure as a proximal boundary condition. Furthermore, out of the same 13 1-D models of the entire systemic circulation, only 2 [Avolio (2) and Fitchett (13)] included a detailed description of the cerebral arterial tree and none included the coronary tree in their model. Viscoelasticity was often neglected except in Fitchett (13) and Avolio (2). Most of the 1-D models included a wall friction approximation based on steady flow (Poiseuille) and neglected convective acceleration, and in the rest of the 1-D models there is a significant disparity in the way wall friction and convective acceleration is approximated. There is also great disparity in the way boundary conditions at the distal termination sites are formulated.

In view of the above, we undertook the present study to construct a 1-D model of the entire arterial circulation that is as complete as possible, i.e., it incorporates a heart model, it includes a detailed description of the cerebral and coronary arterial tree, it models nonlinear and viscoelastic properties of the wall in a physiologically relevant manner, it includes wall friction and convective acceleration effects while respecting the pulsatile nature of the velocity profile, and it provides for realistic distal boundary conditions at the termination sites. This model is subsequently validated against measurements of pressure and flow waves measured in various locations of the arterial tree in a group of young and healthy individuals to qualitatively assess correspondence between model predictions and actual arterial pressure and flow waves.

Address for reprint requests and other correspondence: P. Reymond, Laboratory of Hemodynamics and Cardiovascular Technology, Ecole Polytechnique Fédérale de Lausanne, Switzerland, EPFL/STI/IBI2/LHTC, AI 1231, Station 15, CH-1015 Lausanne, Switzerland (e-mail: philippe.reymond@epfl.ch).

Table 1. *Literature review of distributed one-dimensional models of the systemic arterial tree*

	Reference No.	Heart Model	Complete Systemic Arterial Tree	Cerebral Arterial Tree	Coronary Arteries	Arterial Wall Viscoelasticity	Wall Shear Stress Formulation	Convective Acceleration	Distal Vasculature Models
Bessems et al.	6	−	−	−	−	−	+[c]	+[c]	−
Azer and Peskin	3	−	+	−	−	−	+[a]	+[a]	+[f]
Huo and Kassab	22	−	−	−	+	−	−	−	+[g]
Alastruey et al.	1	−	−	+	−	−	−	−	+[e]
Formaggia et al.	14	+	+	−	−	−	−	+[d]	+[e]
Sherwin et al.	55	−	+	−	−	−	−	−	−
Wan et al.	69	−	−	−	−	−	−	−	−
Olufsen et al.	44	−	+	−	−	−	+[c]	+[c]	+[f]
Cassot et al.	10	−	−	+	−	−	−	−	−
Stergiopulos et al.	64	−	+	−	−	−	+[b]	+[d]	+[e]
Fitchett	13	+	+	+	−	+	−	−	−
Papapanayotou et al.	46	−	−	+	−	−	−	−	−
Hillen et al.	19	−	−	+	−	−	−	−	−
Zagzoule and Marc-Vergnes	74	−	−	+	−	−	−	−	+[h]
Kufahl and Clark	29	−	−	+	−	−	+[c]	+[c]	+[e]
Meister	36	−	+	−	−	−	+[a]	−	−
Stettler et al.	65, 66	−	+	−	−	−	−	−	−
Avolio	2	−	+	+	−	+	−	−	−
Raines et al.	48	−	−	−	−	−	−	+[d]	+[e]
Wemple and Mockros	70	−	+	−	−	−	+[c]	+[c]	−
Schaaf and Abbrecht	50	−	+	−	−	−	+[c]	+[d]	−
Westerhof et al.	71	−	+	−	−	−	−	−	−
Noordergraaf et al.	41	−	+	−	−	−	−	−	−

Heart model: +, presence of a heart model coupled to arterial tree. Complete systemic arterial tree: +, all major arteries of systemic tree are included; −, the model is restricted to specific parts of arterial tree. Cerebral arterial tree: +, detailed description of cerebral arterial tree, including the circle of Willis and smaller efferent vessels; −, cerebral circulation is limited only to major cerebral vessels (i.e., carotids and vertebrals). Coronary arteries: +, presence of coronary arteries in the models; −, total omission of coronary arteries. Arterial wall viscoelasticity: +, modeling of a viscoelastic arterial wall; −, arterial wall is considered elastic. Wall shear stress formulation and convective acceleration: −, wall shear stress is calculated based on mean flow and using Poiseuille's law. [a]Shear stress estimated from the Witzig-Womersley theory for pulsatile flow; [b]Young and Tsai formulation; [c]approximated velocity profiles; [d]flat velocity profile. Distal vasculature models: [e]windkessel 3 elements models (WK3); [f]structured tree from Ref. 43; [g]Womersley impedance; [h]microcirculation and venous system considered.

METHODS

Mathematical Model

Governing equations. Arteries are considered as straight long tapered segments with viscoelastic wall. The 1-D continuity and momentum equations are obtained by integrating the continuity and longitudinal momentum equations of the Navier-Stokes equations:

$$\frac{\partial A}{\partial t} + \frac{\partial Q}{\partial x} + \psi = 0 \tag{1}$$

$$\frac{\partial Q}{\partial t} + \frac{\partial}{\partial x}\left(\int_A u^2 dA\right) = -\frac{A}{\rho}\frac{\partial P}{\partial x} - 2\pi R\frac{\mu}{\rho}\frac{\partial u}{\partial r}\bigg|_{r=R} + Ab_x \tag{2}$$

where $A(x,t)$ is the instantaneous arterial lumen area of radius $R(x,t)$, $u(r,x,t)$ is the longitudinal velocity component, $Q(x,t)$ is the volumetric flow rate (VFR), $P(x,t)$ is the transmural pressure, $\tau_w(x,t)$ is the wall shear stress, b is the body force, and Ψ is the arterial wall seepage. Blood is assumed to be a Newtonian fluid with density ρ and dynamic viscosity μ. *Equations 1* and *2* contain three primary variables (P, *Q*, and A), and thus one more equation is needed to close the system. This is given by the constitutive relation relating distending pressure, P, to local cross-sectional area, A (see *Viscoelastic properties*). The formulation of the momentum equation (*Eq. 2*) contains the convective acceleration term $\left(\frac{\partial}{\partial x}\int_A u^2 dA\right)$ as well as a wall friction term $\left(\tau = \mu\frac{\partial u}{\partial r}\Big|_{r=R}\right)$, both of which depend on the local velocity profile, which is a priori unknown. Approximations to these two terms using the Witzig-Womersley pulsatile theory are discussed below.

Viscoelastic properties of the arterial wall. The arterial wall behavior is nonlinear (elastic modulus depends on distention) and viscoelastic. Following Holenstein et al. (21), we assume that the arterial lumen area at a given location is the sum of a nonlinear elastic, A^e, and viscoelastic, A^v, component, respectively.

$$A(t) = A^e[P(t)] + A^v(t) \tag{3}$$

The elastic component of the local area A^e is related to the instantaneous distending pressure, P, via the local area compliance, C_A^e. The latter is a function of distending pressure but also a function of location. To account for both pressure and location dependence, we assumed that area compliance is the product of the pressure-dependent function, $C_p^e(p)$, and a location-dependant function, $C_d^e(\bar{d}, P_{ref})$, such that

$$C_A^e(\bar{d}, P) = C_d^e(\bar{d}, P_{ref}) \cdot C_p^e(P) \tag{4}$$

$C_d^e(\bar{d}, P_{ref})$ gives the compliance for a given local mean lumen diameter, d, and at a given reference pressure value, here taken as P_{ref} = 100 mmHg. In general, the arterial lumen diameter decreases as we move from the heart toward the periphery and this decrease is accompanied by a decrease in local area compliance; therefore, there is good ground to propose a general $C_d^e(\bar{d}, P_{ref})$ function for all arterial segments. The pressure dependency of the compliance in thoracic and abdominal aortas was measured and determined by (30) to be

$$C_p^e(P) = a_1 + \frac{b_1}{1 + \left[\frac{P - P_{maxC}}{P_{width}}\right]^2} \tag{5}$$

with $a_1 = 0.4$, $b_1 = 5$, $P_{maxC} = 20$ (mmHg), and $P_{width} = 30$ (mmHg) yielding a good functional fit. These parameter values are retained for

the entire arterial tree, assuming that the functional dependence of local area compliance on pressure is approximately the same in all arterial locations.

Most published data in the literature provide for estimates of local pulse wave velocity (PWV) rather than compliance. We therefore derive the values of compliance at the reference pressure from PWV values using the relation:

$$C_d^e(\bar{d}, P_{ref}) = \frac{A}{\rho PWV^2(\bar{d}, P_{ref})} \quad (6)$$

Reported values of PWV in the literature will be represented as a function of the mean arterial lumen diameter to deduce a global empirical relationship based on which compliance at every arterial location will be derived (see *Physiological Data*). To include the viscoelastic component, the model developed by Holenstein et al. (21) is implemented. The viscoelastic behavior is given by the convolution product between the elastic area, A^e, and the derivative of a creep function, $J(t)$.

$$A^v(t) = \int_0^\infty \dot{J}(\tau) A^e[P(t-\tau)]d\tau \quad (7)$$

$$J(\tau) = \tilde{a}\,\frac{e^{-t/\tau_2} - e^{-t/\tau_1}}{t} \quad (8)$$

In Holenstein et al., the values $\tau_1 \cong 0.00081$ s and $\tau_2 \cong 0.41$ s were derived from the published data by Bergel (5). Furthermore, based on Bergel's data for the thoracic aorta, abdominal aorta, and femoral artery, we may assume that the viscoelastic coefficient, $\tilde{a}$, increases linearly as the diameter decreases from heart to periphery. We may thus write

$$\tilde{a} \cong a_3 \cdot \bar{d} + b_3 \quad (9)$$

Considering the elastic and viscoelastic arterial wall components (*Eq. 3*), the continuity equation (*Eq. 1*) is rewritten in the following form:

$$\frac{\partial P}{\partial t} = -\frac{1}{C_A^e}\left[\frac{\partial A^v}{\partial t} + \frac{\partial Q}{\partial x}\right] \quad (10)$$

Wall shear stress and convective acceleration term. Both convective acceleration and wall shear stress depend on the instantaneous velocity profile, which is a priori unknown in the 1-D formulation. Approximations need to be made. Earlier studies have used a number of different approaches for the two terms (see Table 1). Our approach is to use the Witzig-Womersley theory to model as best as possible the pulsatile effects on the velocity profile. Because the Witzig-Womersley theory is obtained in the frequency domain, this requires the knowledge of the local flow waveform over the entire heart cycle. To overcome this inherent difficulty, we assume that the solution is periodic and we use the flow waveform from the previous heart cycle to calculate the velocity profile and the wall shear stress using the relations:

$$u(r,t) = \frac{2}{\pi R^2}\left(1 - \frac{r^2}{R^2}\right)Q_1 + \sum_n Re\left\{\frac{Q_n}{\pi R^2}\,\frac{1 - \frac{J_0(\alpha i^{3/2} r/R)}{J_0(\alpha i^{3/2})}}{1 - \frac{2J_1(\alpha i^{3/2})}{\alpha i^{3/2} J_0(\alpha i^{3/2})}}\,e^{i\omega t}\right\} \quad (11)$$

$$\tau_\omega(t) = -\frac{4\mu}{\pi R^3}Q_1 + \sum_n Re\left\{\frac{\mu}{\pi R^3}Q_n \alpha i^{3/2}\,\frac{J_1(\alpha i^{3/2})}{J_0(\alpha i^{3/2})}\,\frac{1}{1 - \frac{2J_1(\alpha i^{3/2})}{\alpha i^{3/2} J_0(\alpha i^{3/2})}}\,e^{i\omega t}\right\} \quad (12)$$

We solve in time over a number of repeating cycles till convergence. Q is mean flow, $Q_n(z,t)$ is the n^{th} harmonic of the flow pulse, and J_0 and J_1 are the complex Bessel functions of first kind and of zero and first order, respectively. In *Eqs. 11* and *12*, the artery radius, R, is assumed constant and equal to the local radius at mean arterial pressure; α_i is the Womersley number for each harmonic defined as $\alpha_i = R(\rho 2\pi f_i/\mu)^{1/2}$, with f_i being the frequency of the i^{th} harmonic.

Distal vasculature models and boundary conditions at termination sites. Peripheral arterial segments are terminated with a three-element windkessel (WK3) model, which accounts for the cumulative effects of all distal vessels (small arteries, arterioles, and capillaries) beyond a terminal site. The WK3 model accounts for the proximal resistance (R_1), compliance (C_T), and distal resistance (R_2) of the vascular bed. The relation between pressure and flow in the time domain constitutes the distal boundary conditions and is expressed in differential form as:

$$\frac{\partial Q}{\partial t} = \frac{1}{R_1}\frac{\partial P}{\partial t} + \frac{P}{R_1 R_2 C_T} - \left(1 + \frac{R_1}{R_2}\right)\frac{Q}{R_1 C_T} \quad (13)$$

Total peripheral resistances $R_T = R_1 + R_2$ are estimated based on measured mean flow distribution in the major arterial beds (see *In Vivo Measurements*). For terminal arterial segments where flow rate is not measured or available, we completed the values assuming that the mean wall shear stress (given by Poiseuille's law) is the same as for nearby arteries. To define the values of the proximal (R_1) and distal (R_2) resistances, we further assume that the wave reflections at terminal sites vanish at high frequencies. A reflection coefficient at the distal interface is defined as

$$\Gamma(f) = \frac{Z_T(f) - Z_C}{Z_T(f) + Z_C} \quad (14)$$

where $Z_C = \rho \cdot PWV/A$ is the characteristic impedance of the last arterial segment proximal to the terminal WK3. Reflections at high frequencies vanish when $Z_C = |Z_T|$. At high frequencies, the modulus of the WK3 tends toward the value of its equal to its proximal resistance ($|Z_T| = R_1$). Hence, the condition for minimal reflection at high frequencies is $R_1 = Z_C$. Distal resistance is then obtained as $R_2 = R_T - R_1$. In the case of the present arterial tree, the minimal reflection at high frequencies implies that the ratio R_1-to-R_T varies in the range of [0.05–0.4], compared with a fixed value of 0.2 arbitrarily chosen in previous studies (48, 64). To respect the continuity in elastic properties of the terminal vessels, the windkessel compliance, C_{Ti}, is assumed to be proportional to the area compliance, C_A^i, of the terminal vessel at its distal end:

$$C_T^i \cong C_T \frac{C_A^i}{\sum C_A^i} \quad (15)$$

where $C_T = \sum_i C_T^i$ is the part of the total volume compliance attributed to peripheral vessels beyond the termination sites.

Arterial bifurcations. We impose continuity of pressure and flow across each branching point, neglecting thus any minor pressure losses occurring in the vicinity of the bifurcation. Earlier wave reflection analysis on the original Noordergraaf/Westerhof tree (71), subsequently modified by Stergiopulos et al. (64) has shown that significant nonphysiological reflections arise in the aorta and that this is primarily due to rather high reflection coefficients at various bifurcations along the aorta (F. Merenda, unpublished observations). Papageorgiou et al. (45) studied wave reflections along the aorta and concluded that the main arterial junctions are well matched for minimizing forward wave's reflections. The forward wave reflection coefficient at an arterial bifurcation is given by:

$$\Gamma = \frac{Z_{upstream}^{-1} - \sum Z_{downstream}^{-1}}{Z_{upstream}^{-1} + \sum Z_{downstream}^{-1}} \quad (16)$$

where Z is the characteristic impedance of the upstream and downstream vessels. To minimize forward wave reflections, we chose to adapt the characteristic impedance of the downstream branches, so that the absolute value of the reflection coefficient given by *Eq. 16* is always <0.1. This is achieved by slightly adjusting the cross sectional area of the daughter branches, while keeping the arterial wall distensibility unchanged.

Heart model. At its proximal end (root of the ascending aorta), the arterial tree is coupled to a model of the LV. The LV is modeled using the varying elastance model, as suggested by Sagawa (49). The varying elastance model is based on the time varying elastance [$E(t)$] of the left ventricle, which describes the variation of LV pressure (P_{LV}) and volume (V_{LV}) during a cardiac cycle:

$$E(t) = \frac{P_{LV}(t)}{V_{LV}(t) - V_0} \quad (17)$$

where V_0 is the dead volume of the LV (Fig. 1*A*). Figure 1*A* also shows the four phases of the cardiac cycle, and it is to be noted that under physiological conditions (no leaky valves) only during ejection (*phase II* on Fig. 1*A*) there is interaction between the LV and the arterial tree. Figure 1*B* shows the normalized varying elastance curve for one heart cycle. According to Senzaki et al. (54), the normalized varying elastance curve is relatively invariable in young and old subjects and is relatively unaffected by various forms of disease. Hence, the varying elastance curve for any individual is fully determined by only three cardiac parameters, i.e., the maximal elastance (E_{max}), the minimal elastance (E_{min}), and the time to maximum elastance (t_{max}).

During ejection, the aortic valve is open and thus reflected waves traveling backwards in the aorta will be reflected according to the impedance mismatch between the proximal aorta and the left ventricle. Earlier studies (8, 56) have pointed out that modeling the ventricle as a purely compliant chamber yields nonphysiological wave reflection for the backward running waves and suggested the introduction of an internal LV resistance in series to its compliance to improve the wave reflection characteristics of the left ventricle. The internal resistance R_{int} was introduced to explain, phenomenologically, the observed difference in the ventricular pressure of an ejecting heart (P_{LV}) and the ventricular pressure during an isovolumic contraction P_{LV}^* (Fig. 1*B*). Hence, in an ejecting heart ventricular pressure is equal to P_{LV}^* minus the pressure drop over the internal resistance:

$$P_{LV} = P_{LV}^* - R_{int}(t)Q(t) \quad (18)$$

Experimental evidence showed that internal resistance is itself proportional to P_{LV}^*, so that

$$R_{int}(t) = \kappa P_{LV}^* \quad (19)$$

Taking the above into consideration, we derive the following expression for the varying elastance of an ejecting heart:

$$E(t) = E^*(t)[1 - \kappa Q(t)] \quad (20)$$

where E^* represents the elastance that would be measured during an isovolumic (nonejecting) contraction. *Equation 20* allowed us to reconstruct a normalized isovolumic elastance, E^*, from the normalized elastance curves, E, reported by (54; Fig. 1*B*) and from aortic flow waves measured in vivo (see *Heart model* in *Physiological Data*).

Coronary model. Main coronary arteries are modeled assuming a systolic flow impediment, which is proportional to the varying elastance. The coronary vessel diameter and compliance are affected by the contraction of the myocardium. Epicardial vessels are affected differently from endocardial and subendocardial vessels, but for the sake of simplicity, we follow here the approach of Vis et al. (68) and assume that compliance and resistance changes are proportional to the local time varying elastance of each vessel, which, according to Krams et al. (27), is assumed to have the same wave shape as the varying elastance of the left ventricle. Hence, we may express the contraction-induced changes in vessel wall distensibility (D_w) and terminal windkessel properties (R_1, R_2, and C_T) as follows:

$$\begin{aligned} D_w(E(t)) &\approx D_w^{ref} - \varepsilon D_w^{ref} E(t)/E_{max} \\ C_T(E(t)) &\approx C_T^{ref} - \alpha C_T^{ref} E(t)/E_{max} \\ R_1(E(t)) &\approx R_1 + \beta R_1 E(t)/E_{max} \\ R_2 &\approx \delta R_1 \end{aligned} \quad (21)$$

where ε, α, β, and δ are constants of proportionality. These relations are applied to the left coronary arteries. For the right coronaries, we assume that the effect of the right ventricle contraction is smaller by a factor proportional to the ratio of maximal pressure in the two ventricles, taken as $P_{LV,max}/P_{RV,max} \approx 6$.

Numerical solution. The set of equations with the boundary conditions described above is solved using an implicit finite difference scheme to yield pressure and flow waveforms over the entire arterial tree. Nonlinear terms are iteratively solved at each time step using the Newton-Raphson method. We initialize the arterial with an arbitrary pressure of 100 mmHg and a flow of 1 ml/s in each artery, the solution being quite insensitive to the initial distribution of pressure and flow and always converging. Our convergence criterion is based on the maximum relative difference of 1% in pressure and flow between two consecutives cardiac cycles for all nodes and all time steps within the cardiac cycle.

Physiological Data

Geometry. The arterial tree dimensions are based on the original Noordergraaf tree (40), which was later adapted by Westerhof et al. (71) and by Stergiopulos et al. (64; Fig. 2*A*). Because the Stergiopulos et al. tree did not provide for a detailed description of the cerebral circulation, we added the main afferent and efferent vessels in the vicinity of the circle of Willis, as shown in Fig. 2*D*. The considered circle of Willis is assumed to be complete, although representative of only (42%) of the population (26) due to significant anatomical

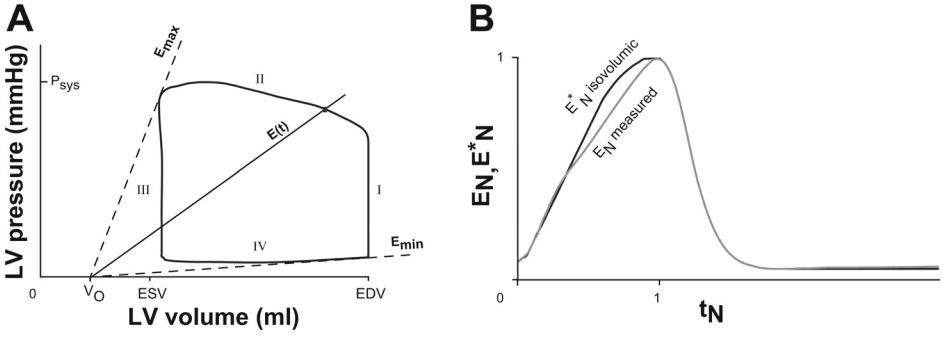

Fig. 1. *A*: A heart cycle represented as a ventricular pressure-volume graph. Instantaneous elastance, maximum elastance (E_{max}) and minimal elastance (E_{min}) are also represented. E_{max} intersects the left ventricular (LV) volume axis at the dead volume abscissa (V_0). *B*: normalized time varying elastance (E_N, E_N^*) as function of normalized time. EDV and ESV, end diastolic and end systolic developed pressure; $E(t)$, time varying elastance; P_{sys}, systolic pressure.

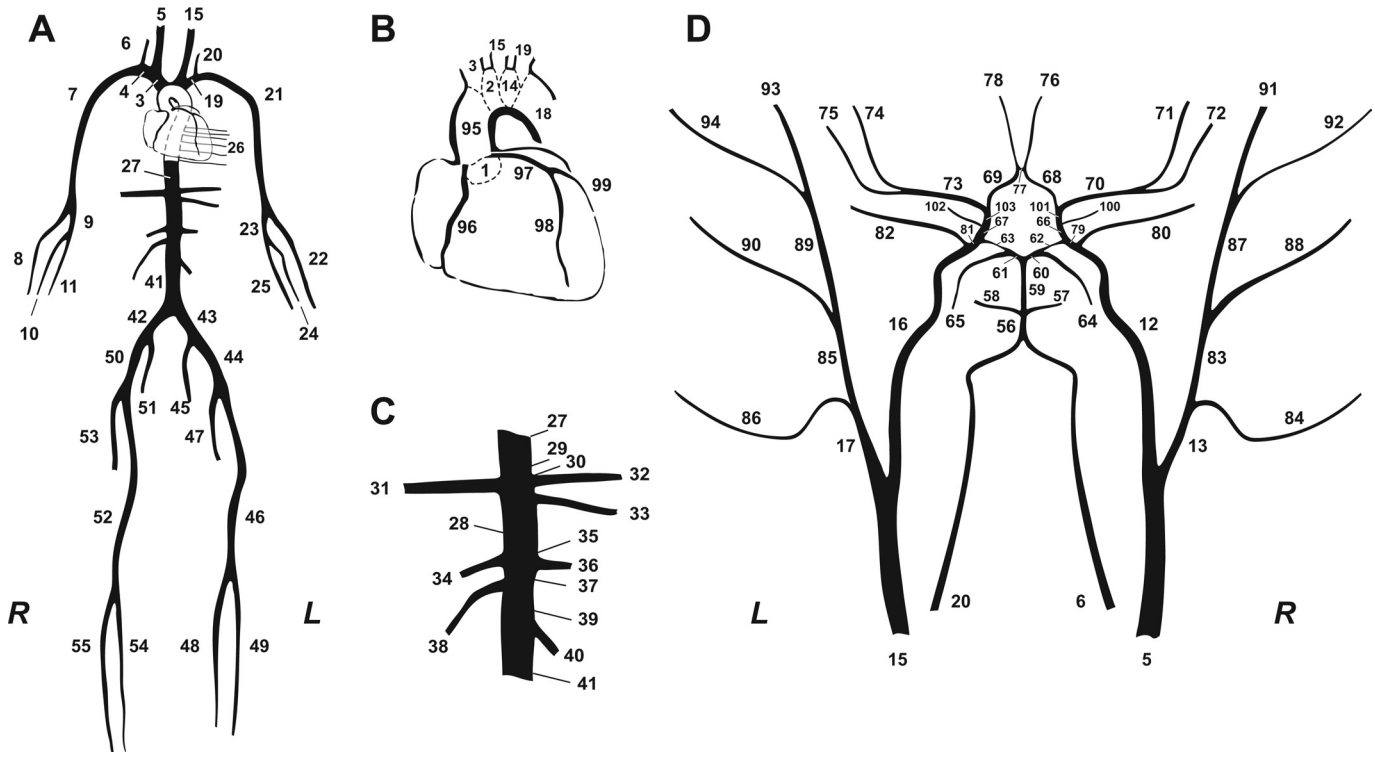

Fig. 2. Schematic representation of the arterial tree. *A*: main systemic arterial tree, based on the model of Stergiopulos et al. (64). *B*: detail of the aortic arch and the coronary network. *C*: detail of the principal abdominal aorta branches. *D*: blown-up schematic of the detailed cerebral arterial tree, which is connected via the carotids (*segments 5* and *15*) and the vertebrals (*segments 6* and *20*) to the main arterial tree shown in *A*. R, right; L, left.

variations from subject to subject. The geometry of the main cerebral arteries was obtained from averaged literature data (Table 2) and completed by real patient scans (3DRA and MRA). Many extracranial arteries, such as the superficial temporal arteries, have also been added to include points where pressure can be measured noninvasively (tonometry), which is required for the validation phase of the work. The secondary anastomoses, such as the internal-external carotid, subclavian-carotid, and subclavian-vertebral are not considered.

The Stergiopulos et al. (64) arterial tree model did not include the coronaries. Because the coronary circulation is particular and perhaps not well adapted to the 1-D model description, we decided to limit ourselves only to simplified description of the coronary tree, where only the main coronary arteries are included (Fig. 2*B*).

Blood rheological invariable parameters in the current study are as follows: $\rho = 1{,}050$ (kg/m^3) and $\mu = 0.004$ (Pa·s).

We assume an impermeable arterial wall ($\Psi = 0$).

Elastic properties. The values of PWV reported in the literature for different arteries as a function of the mean arterial lumen diameter are presented in Fig. 3. We observe that, despite some well-anticipated dispersion, there is a general trend of an inverse global relation between artery size and PWV. To that effect, we fitted an empirical inverse power curve:

$$\mathrm{PWV}(\bar{d}) \approx \frac{a_2}{\bar{d}^{b_2}} \qquad (22)$$

This simple empirical relation seems to be sufficiently well adapted, especially for large arteries with a lumen diameter >5 mm. For smaller arteries, encountered for instance in the vicinity of the circle of Willis, it seems to underestimate the PWV. The coefficients obtained from the best fit are $a_2 = 13.3$, $b_2 = 0.3$, with $R^2 = 0.6$.

For intracranial arteries that are surrounded by the cerebrospinal fluid (CSF), we assume that the CSF mean pressure is of 15 mmHg and acts on the outer surface of the arterial wall. This implies that the distending pressure, which is lumen pressure minus external pressure, is decreased and thus the arterial wall compliance is increased (*Eq. 5*).

Viscoelastic properties. The linear viscoelastic coefficient, $\tilde{a}$, was obtained by fitting *Eq. 9* on the viscoelasticity data reported by (5). The best-fit yielded $a_3 = -0.0062$ (mm^{-1}) and $b_3 = 0.16$ ($R^2 = 0.90$). For cerebral arteries, which present a much stronger viscoelastic component [Bergel et al. (5)], only one point that corresponds to the carotid artery was available; therefore, we assumed same slope (a_3) as for the other arteries. However, the parameter b_3 was taken as $b_3 = 0.34$ to match the carotid viscoelasticity value.

Vascular resistance and compliance. Peripheral resistances were based on data by Stergiopulos et al. (64). For the cerebral circulation, which was not included in the Stergiopulos et al. model, we derived peripheral resistances from mean flow data published in the literature or from our own flow measurements (Table 3).

The total systemic vascular compliance is the sum of the volume compliances of all vessels including also the compliance of the terminal beds, so that $C_v = \Sigma_n^i C_{v,i} + \Sigma_m^i C_{\mathrm{T},i}$, where $n = 103$ is the number of arterial segments and $m = 47$ is the number of terminal beds. The volume compliance of each arterial segment is obtained by integrating the area compliance (*Eq. 5*) over the segment length. Volume compliances were finally adjusted so that the total systemic compliance matches literature values for a typical young healthy subject of the same age as the average age of our subject group. More than 50% of the total arterial compliance is in the aorta (23), and thus only a minor part is attributed to peripheral beds. We here follow Stergiopulos et al. (64) and assume that the sum of compliances of the terminal beds is in the order of 20% of the total systemic compliance.

Heart model. We derived isovolumic elastance (E^* in *Eq. 20*) from the global normalized elastance curve (E) reported by Senzaki et al. (54; Fig. 1*B*). This required the use of a "standard" aortic flow waveform, which we obtained by averaging our own measurements with phase-contrast (PC)-MRI at the ascending aorta of a group of

Table 2. *Geometry, distensibility, viscoelastic properties, and peripheral resistances and compliances of the arterial tree*

Arterial Segment Name	Arterial Segment Number (Right/Left)	Arterial Segment Length, mm	Proximal Lumen Diameter, mm	Distal Lumen Diameter, mm	Distensibility, 10^{-3} l/mmHg	Viscelasticity coeff. (ã)	Terminal Resistance ($R_1 + R_2$), mmHg·s·ml^{-1}	Terminal Compliance (C_T), 10-5 ml/mmHg
Ascending aorta 1	1	5	29.4	29.3	5.46	0.05		
Aortic arch A	2	20	25.1	24.0	4.90	0.05		
Brachiocephalic	3	34	20.2	18.0	4.22	0.05		
Subclavian A	4/19	34	11.5/11.0	9.0/8.5	2.90/2.81	0.09/0.10		
Common carotid	5/15	94/139[h]	13.5/12.0	7.0/6.0[e]	2.93/2.68	0.09/0.10		
Vertebral	6/20	149/148	3.7[d,i,j]	2.8[c]	1.46	0.14		
Subclavian B, axillary, brachial	7/21	422	8.1	4.7	2.19	0.12		
Radial	8/22	235	3.7/3.5	3.1/2.8	1.49/1.43	0.14	39.7	702.9
Ulnar A	9/23	67	3.7/4.3	3.4/4.3	1.53/1.72	0.14/0.13		
Interosseous	10/24	79	2.1/1.8	1.8	1.08/1.03	0.14/0.15	633.8	44.0
Ulnar B	11/25	171	3.2/4.1	2.8/3.7	1.39/1.62	0.14/0.13	39.7	702.9
Internal carotid	12/16	178	5.7/5.3[d,i,j]	4.3/4.1[c,i]	1.89/1.82	0.13		
External carotid 1	13/17	41[h]	5.0/4.7	4.5/4.3	1.83/1.77	0.13		
Aortic arch B	14	39	21.4	20.8	4.48	0.05		
Thoracic aorta A	18	52	20.0	18.9	4.26	0.05		
Intercostals	26	80	12.6	9.5	3.04	0.09	10.5	2670.1
Thoracic aorta B	27	104	16.5	12.9	3.60	0.07		
Abdominal aorta A	28	53	12.2	12.2	3.22	0.08		
Celiac A	29	20	7.8	6.9	2.38	0.11		
Celiac B	30	20	5.2	4.9	1.90	0.13		
Hepatic	31	66	5.4	4.4	1.87	0.13	27.3	1022.5
Gastric	32	71	3.2	3.0	1.42	0.14	40.7	686.1
Splenic	33	63	4.2	3.9	1.66	0.13	17.4	1599.8
Superior mesenteric	34	59	7.9	7.1	2.41	0.11	7.0	3991.0
Abdominal aorta B	35	20	11.5	11.3	3.09	0.09		
Renal	36/38	32	5.2	5.2	1.93	0.12	8.5	3284.6
Abdominal aorta C	37	20	11.8	11.8	3.16	0.08		
Abdominal aorta D	39	106	11.6	11.0	3.07	0.09		
Inferior mesenteric	40	50	4.7	3.2	1.64	0.13	51.7	539.5
Abdominal aorta E	41	20	10.8	10.4	2.96	0.09		
Common iliac	42/43	59	7.9	7.0	2.39	0.11		
External iliac	44/50	144	6.4	6.1	2.15	0.12		
Inner iliac	45/51	50	4.0	4.0	1.65	0.13	59.7	467.7
Femoral	46/52	443	5.2	3.8	1.77	0.13		
Deep femoral	47/53	126	4.0	3.7	1.61	0.13	35.9	778.1
Posterior tibial	48/54	321	3.1	2.8	1.38	0.14	35.9	778.1
Anterior tibial	49/55	343	2.6	2.3	1.24	0.14	42.0	664.0
Basilar artery 2	56	20	4.0[d,j,]	3.6	1.60	0.31		
Superior cerebellar	57/58	10	1.7[j]	1.4	0.93	0.33	200.8	3.6
Basilar artery 1	59	5	3.1[f]	2.7	1.36	0.32		
Post. cerebral 1	60/61	2	1.9[c,d,f,j]	1.9	1.05	0.33		
Post. communicating	62/63	4	1.2[c,f,j]	1.2	0.78	0.33		
Post. cerebral 2	64/65	59	2.0[f]	1.8	1.12	0.32	80.5	5.8
ICA distal PCo–ant. chor. seg.	66/67	2	3.9	3.8	1.62	0.31		
Ant. cerebral 1	68/69	12	2.1[c,d,f,h,j]	2.0	1.10	0.32		
Middle cerebral M1	70/73	8	3.0[c,f,j]	2.8	1.36	0.32		
MCA M2 sup. fr. cist. sylvian bif.	71/74	71	2.0	1.0	0.92	0.33	75.2	2.8
MCA M2 inf. br. dist. sylvian bif.	72/75	70	2.0	1.0	0.92	0.33	75.2	2.8
Ant. cerebral A2	76/78	24	1.8	1.7	0.99	0.33	80.5	4.7
Ant. communicating	77	2	1.3[f,i,j]	1.3	0.84	0.33		
Int. car. sinus	79/81	11	4.3	3.9	1.67	0.31		
Ophthalmic	80/82	11	1.0[i]	0.5	0.60	0.33	200.8	0.4
External carotid 2	83/85	61	4.0	3.5	1.59	0.13		
Sup. thy. asc. ph. lyng. fac. occ.	84/86	101	2.0	1.0	0.92	0.15	225.6	5.9
Superficial temporal	87/89	61	3.2	3.0	1.42	0.14		
Maxillary	88/90	91	2.2	1.0	0.95	0.15	188.0	5.0
Superficial temporal frontal br.	91/93	100	2.2	1.4	1.02	0.15	188.0	8.2
Superficial temporal parietal br.	92/94	101	2.2	1.4	1.02	0.15	188.0	7.6
Ascending aorta 2	95	35	29.3	28.8	5.42	0.05		
Right coronary RCA	96	53.7[g]	3.6[a]	2.6[a]	1.42	0.14	55.6	26.6
Left main coronary LCA	97	5[a]	4.9	4.7	1.84	0.13		
Left anterior descending cororanry LAD	98	47[g]	3.8[a]	1.5[a]	1.29	0.14	45.1	26.6
Left circumflex LCx	99	26[g]	3.5[a]	3.1[a]	1.47	0.14	45.1	26.6
Ant. choroidal	100/102	36	1.5	1.3	0.88	0.15	150.4	15.4
ICA distal cnt. chor.–M1 seg.	101/103	2	3.8	3.8	1.61	0.13		

Given arterial wall distensibility and lumen radius are assumed values for a reference transmural pressure of 100 mmHg. ICA, internal carotid artery; MCA, middle cerebral artery; LCA and RCA, left and right carotid artery; LCx, left circumflex coronary artery. [a]Dodge et al. (11); [b]Fox et al. (15); [c]Gabrielsen and Greitz (16); [d]Hillen et al. (19); [e]Holdsworth et al. (20); [f]Krabbe-Hartkamp et al. (26); [g]Pennell et al. (47); [h]Krayenbuehl and Yasargil (28); [i]Yasargil (73); [j]data from G. P. B. Wollschlaeger summarized by Yasargil (73).

young volunteers (see *In Vivo Measurements*). The value of κ was derived by minimizing the difference between the resulting elastance of the 1-D model run and the original one from Senzaki et al. (54). This yields $\kappa = 0.0005$ (s/ml).

The main parameters of the heart model were taken from a study by Merenda (37), who examined the influence of each parameter on the waveforms in the ascending aorta. Heart parameters yielding physiologically relevant aortic pressure and flows for young adults pressure

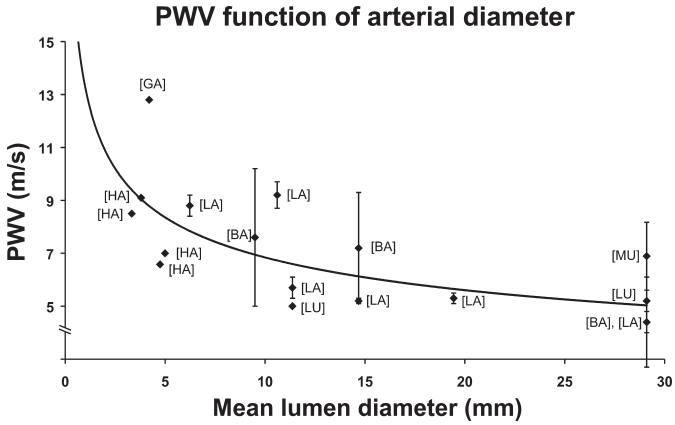

Fig. 3. Pulse wave velocity (PWV) reported in the literature for different arteries, plotted as a function of the arterial lumen diameter. Acronyms refer to the publication from which the specific data points were extracted [BA, Baguet et al. (4); GA, Giller and Aaslid (17); HA, Hayashi et al. (18); LA, Latham et al. (31); LU, Luchsinger et al. (32); MU, Murgo et al. (38)]. Only available SD are shown.

were in the following range: $V_0 = [-50, 300]$ ml, $E_{min} = [0.03, 0.2]$ mmHg/ml, $E_{max} = [1.0–6.0]$ mmHg/ml, end diastolic pressure ($P_{END\text{-}DIA}$) = [5–25] mmHg and venous resistance (R_{ven}) = [0.001–0.003] mmHg·s·ml^{-1}. The reference values chosen for the present study were $V_0 = 15$ ml, $E_{min} = 0.08$ mmHg/ml, $E_{max} = 2.6$ mmHg/ml, $P_{END\text{-}DIA} = 14$ mmHg (54), and venous resistance (R_{ven}) = 0.003 mmHg·s·ml^{-1}. The heart rate is chosen to be 75 bpm, corresponding to average data for a 25 yrs old subject (39). The time to maximum elastance is set to $t_{max} = 340$ ms, this being the average value between our own measurements and those published by (58), who reported a t_{max} range from 262 to 383 ms for subjects 36–60 yr old.

In Vivo Measurements

To validate the 1-D model predictions, we performed noninvasive pressure and flow measurements in young healthy volunteers, aged 15–30 yrs old, at the Geneva University Hospital (HUG). The measurements were performed according to a protocol approved by the local ethics committee. All the volunteers provided written, informed consent. Volume flow rate waveforms were obtained in a first group of patients in systemic arteries using gated PC-MRI. In a second group of patients, flow was measured in precerebral and cerebral arteries using B-mode and color-coded duplex flow imaging. In a subgroup of this second group of patients, pressure waveforms were measured on superficial arteries using applanation tonometry. The foot of the end diastolic flow waveform was set as reference for time alignment of cardiac cycles for inter-volunteer data averaging.

Blood flow measurement using PC-MRI. Two-dimensional PC-MRI sequences (slice thickness = 6 mm, Te/Tr = 3.3/51.7 ms, flip angle = 20°, field of view = 220 × 320 mm; Siemens Trio-Tim 3T System) were acquired at five different large artery sites (Fig. 4) on volunteers [$n = 6$, male/female (4/2), age 28 ± 1.3 (means ± SD), height = 178 ± 12 cm] at rest and in basal conditions. The measurements planes were determined using flash angiography images to ensure that the plane was perpendicular to the vessel axis.

For aortic measurements, breathold sequences were run during 19 s to minimize movement artifacts. Twenty gated phase and magnitude images were acquired, gating being based on pressure pulse measured in the index finger. Arterial cross sections were manually segmented (Argus Flow software, Siemens) to follow lumen area changes over the heart cycle. The volume flow rate was the integral of the velocities across the lumen.

Blood flow measurement using color-coded duplex ultrasound. Color-coded duplex flow imaging with a 5- to 8-MHz linear phase array and a 2- to 4-MHz sectorial transducer were used to assess blood flow velocities in the cerebral vasculature (Toshiba medical device, Aplio 80). Color-coded duplex flow imaging was performed via the temporal, orbital, and occipital acoustic bone windows. Insonation angle was close to 60°, except for the middle cerebral artery where the angle was close to 0°. Diameter values of extracranial arteries were obtained using M-mode imaging. The subjects [$n = 8$, male/female (4/4), age 26 ± 4] were measured at rest at basal conditions and in the supine position. Two subjects were not included, because their examination showed inconstant cardiac cycle periods.

Pressure measurements using applanation tonometry. Pressure waveforms over 10 heart cycles were acquired on the distal radial artery, distal common carotid artery, and temporal arteries (Figs. 4 and 5) with applanation tonometry (SPT 301; Millar Instruments, Houston, TX) on basal conditions and supine positions [$n = 5$, male/female (3/2) age 29 ± 3]. Pressure was calibrated with brachial pressure measured with a sphygmomanometer, based on the assumption that mean and diastolic pressures do not vary much between the brachial artery and the carotid, radial and temporal locations.

Mean sphygmomanometer pressure is calculated as $P_{mean} \cong P_{diastole} + 1/3\ PP$ (52), where PP is the pulse pressure ($P_{systole} - P_{diastole}$).

RESULTS

Model Predictions vs. In Vivo Measurements

PC-MRI flow measurements of flow in the main aortic segments (ascending aorta, thoracic aorta, and abdominal aorta) and main lower limb arteries (common iliac and femoral

Table 3. *Mean flow rate for different cerebral arteries from literature and own measurements*

References	Modality	Age	CCA Left/Right	ICA Left/ Right	ECA Left/Right	MCA Left/Right	ACA Left/Right	PCA Left/Right	VA Left/Right	BA	CBF
Enzmann et al. (12)	cine PC-MR	22–38				1.8/2.1	1.25/1.47	0.88/0.85		2.68	
Buijs et al. (7)	2D PC-MRA	19–29		5.1/4.9						2.53	12.5
Spilt et al. (57)	PC-MRI	18–26 (2nd gr.)									12.6
Scheel et al. (51)	Color duplex	20–39									12.5
Holdsworth et al. (20)	Doppler	24–34	6.0								
Stock et al. (67)	PC-MR	<30				2.1±0.5					
Marshall et al. (33)	cine PC-MR	29±7	6.16	4.14	1.59						
Obata et al. (42)	PC-MRI	18–65		3.8±1.4/3.7±1.0						2.37±0.97	10.3±2.1
Hillen et al. (19)	model*					2.78	1.39	2.08			
Ultrasound		15–30	4.9/6.5	3.7/4.5	2.5/2.7	2.2	1.0		1.2	1.9	
Mean flow rate chosen†			6.0	4.5	1.5	2.5	1.25	1.0			12.5

Values are means (ml/s) ± SE. *Assuming that resistances are inversely proportional to irrigated brain mass. †Averaged mean flow rate of the one-dimensional model to set the distal WK3 resistances in the efferent vessels of the circle of Willis. CCA, common carotid artery; ECA, external carotid artery; ACA, anterior cerebral artery; PCA, posterior cerebral artery; VA, vertebral artery; BA, basilar artery; CBF, cerebral blood flow; PC, phase contrast.

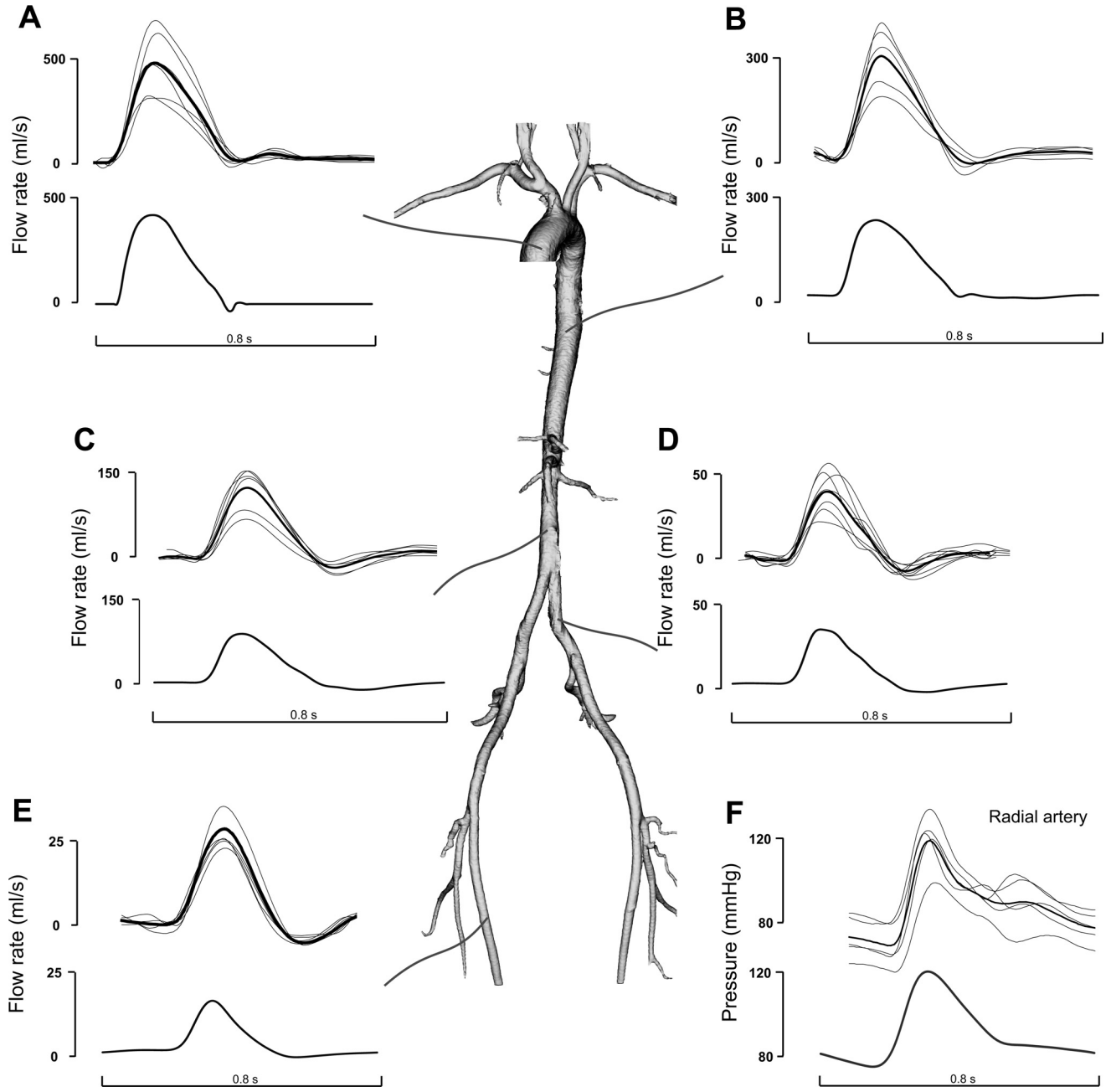

Fig. 4. *A*: ascending aorta. *B*: thoracic aorta. *C*: abdominal aorta. *D*: common iliac. *E*: femoral artery. *F*: radial artery. Model results (*bottom*) compared with in vivo measurements of flow and pressure waves (*top*) at various systemic arteries locations. Thick line represents the averaged waveform. Flow rate waveforms were not available due to poor quality measurements for *volunteer 4* in *B*, *volunteer 1* in *D*, and *volunteers 5* and *6* in *D* and *E*.

artery) are shown in (Fig. 4, *top*). Figure 4*F* includes also pressure measurements in the radial artery. All pulses are plotted in their natural time scale. Model predictions at the same arterial sites are shown in the corresponding lower panels. We observed a good overall agreement in both amplitude and wave shape at all arterial locations. A comparison between predicted and measured maximal, minimal, and mean flow is given in Table 4. Table 5 also gives the comparison for systolic, diastolic, mean, and pulse pressure. The discrepancies are typically of 22 ± 16% (means ± SD) for peak systolic flow and 12 ± 11% for mean flow, whereas they are 9 ± 6% for systolic pressure and 12 ± 5% for diastolic pressure.

Cerebral artery flow waveforms predicted by the model are compared with ultrasound measurements in the middle cerebral artery, vertebral artery, internal carotid artery, and common carotid artery in Fig. 5. Pressure waveforms were measured with applanation tonometry and compared with model predictions in the superficial temporal artery (Fig. 5*B*) and common carotid (Fig. 5*F*). As mentioned in MATERIALS AND METHODS, cerebral blood flow measurements are based on pulsed Doppler data velocities and an "average" local vessel lumen diameter. This means that the absolute values for flow obtained experimentally may contain a significant error, whereas the shape of the flow waveform is rather accurately captured by the Doppler

Table 4. *Quantification of blood flow rate of in vivo measurements and model results at different arteries*

	Systolic Flow Rate, ml/s		Diastolic Flow Rate, ml/s		Mean Flow Rate, ml/s	
	In vivo measurements	Model	In vivo measurements	Model	In vivo measurements	Model
Ascending aorta	470	420	0.5	−33	103	96
Thoracic aorta	303	235	−2.5	14	68	71
Abdominal aorta*	123	87	−21	−10	20	18
Iliac artery	38	34	−7.5	−2.4	7.5	7.8
Femoral artery	28	17	−5.7	−0.3	5.1	3.8
CCA	22	22	2.5	0.7	6.5	5.4
ICA	9.0	9.8	2.2	2.7	3.6	3.9
VA	2.4	2.9	0.8	0.8	1.2	1.2
MCA	3.9	2.7	1.7	1.5	2.5	1.9

*Infra renal level.

ultrasound. Indeed, the similarity in the flow wave shape between model and measurements is quite evident (Fig. 5, *A*, *C*, *D*, and *E*), with all primary and secondary wave shape features being captured quite well.

Effects of Viscoelasticity, Convective Acceleration, and Wall Friction Formulation

Table 6 quantifies the effects of adding viscoelasticity and applying Witzig-Womersley's theory to derive more accurate expressions of convective acceleration and wall shear stress. Differences in pressure and flow waveforms with respect to the "control" model are reported as the root mean square of the difference over the entire heart cycle in three representatives arteries (thoracic aorta, common iliac artery, and middle cerebral artery). As a control model, we take the same 1-D model but without viscoelastic effects and with convective acceleration and wall shear stress being estimated using a quasi-steady parabolic profile. We observe that viscoelasticity as well as convective acceleration and wall friction impact in a significant manner on the flow waveform, in all three arterial sites. The effect on pressure is only important in the peripheral sites (common iliac and middle cerebral artery) but not in the aorta.

Model Predictions in Presence of Detailed Cerebral Circulation

To assess the importance of having a detailed description of the cerebral arterial tree, we examined the predicted pressure and flow waves at two arterial locations: the common carotid artery, which feeds into the cerebral circulation and thus is susceptible to reflected waves coming back from the distal cerebral sites, and the thoracic aorta, which is expected not to be directly affected by the cerebral vasculature. As a control, we take a simple description of the cerebral tree as given in the model by Stergiopulos et al. (Fig. 2*A*; Ref. 64). To preserve equivalence in terms of the global wave propagation and reflection properties, the distal sites of internal and external carotids and vertebral arteries of the "control" model were terminated by lumped WK3 providing the same total terminal resistance and compliance as the detailed cerebral arterial tree model. The results are shown in Fig. 6. We observe considerable differences in the carotid pressure and flow waveforms, the differences in flow being substantial in both amplitude and wave shape. We notice, in particular, that in presence of the detailed cerebral tree, the computed flow exhibits a physiological pulsatility and only forward flow throughout the heart cycle. In the absence of the detailed cerebral tree, the predicted common carotid flow exhibits an abnormally high pulsatility and a nonphysiological backflow at the dicrotic notch (compare also with in vivo measurement in Fig. 5).

DISCUSSION

This study aimed in achieving two goals: first, to improve the 1-D model of Stergiopulos et al. that we developed earlier (64) and that we have successfully utilized as a research tool in a number of subsequent studies (59–63, 72); and second, to validate, at least in a semiquantitative sense, the predictions of the 1-D model with in vivo measurements of pressure and flow. The improvements were carried on at different levels. We included a heart model, we included a simple coronary model, we extended the cerebral circulation to include all major vessels, we added viscoelasticity onto the nonlinear elastic properties of vessel wall, and we improved the description of the convective acceleration and friction terms by employing the Witzig-Womersley theory. Our results showed that the implemented improvements were important and in specific cases, such as the description of cerebral hemodynamics, essential. The validation was carried out by comparing our generic model predictions with average pressure and flow measured in a group of young subjects at different arterial locations. The validation was done by a quantitative comparison of systolic, diastolic, and mean pressure and flow as well as by a qualitative comparison of the shape and features of pressure and flow waveforms. Despite its generic character, the 1-D model provided pressure flow predictions that faithfully reproduced the wave characteristics in all arterial locations and

Table 5. *Quantification of pressure of in vivo measurements and model results at different arteries*

	Systolic Pressure, mmHg		Diastolic Pressure, mmHg		Mean Pressure, mmHg		Pulse Pressure, mmHg	
	In vivo measures	Model	In vivo measures	Model	In vivo measures	Model	In vivo measures	Model
Radial artery	122	125	69	74	87	90	53	51
CCA	101	115	68	81	85	97	33	34
Superficial temporal artery	106	119	71	79	87	96	35	40

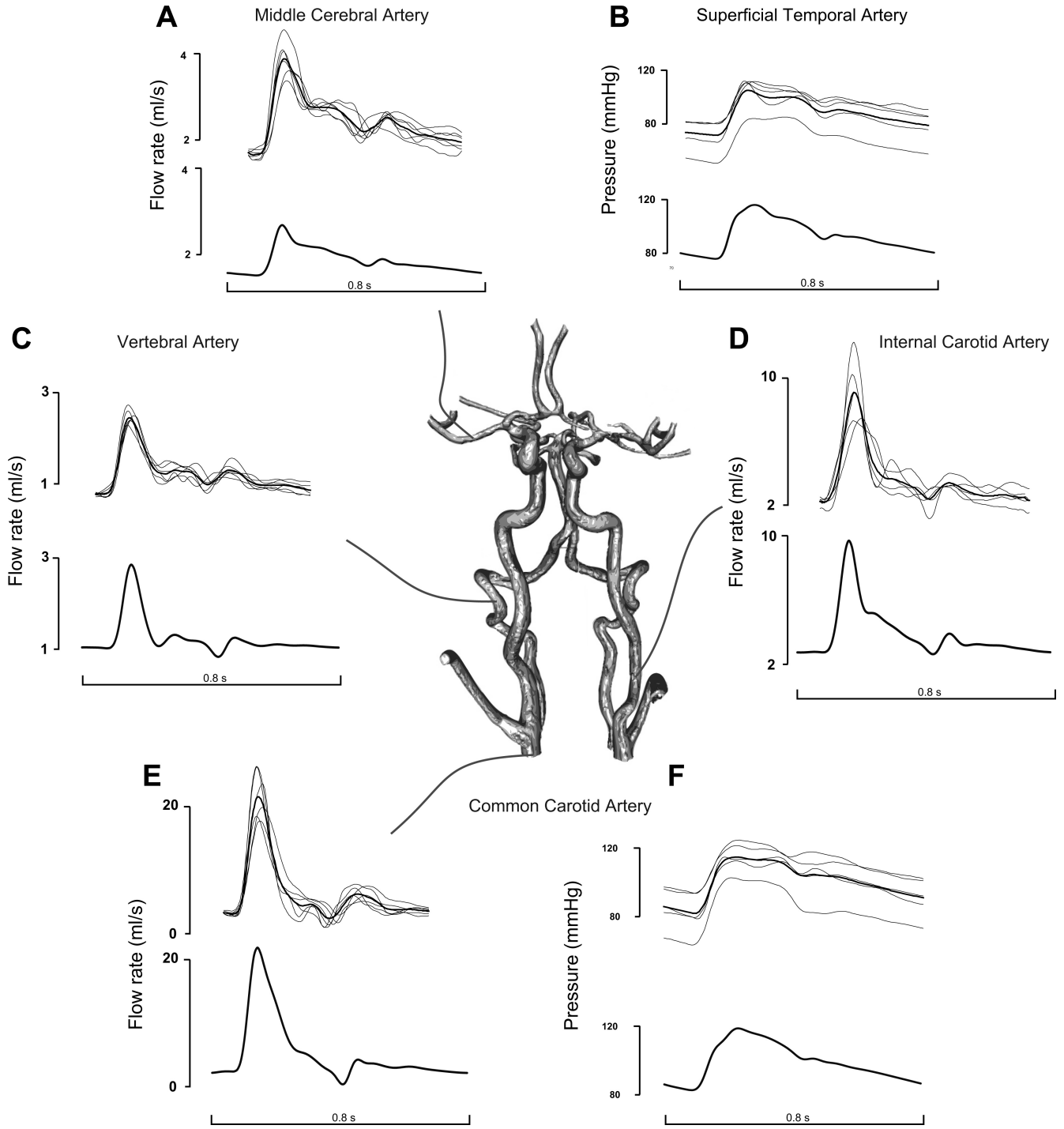

Fig. 5. Model results (*bottom*) compared with in vivo measurements of flow and pressure waves (top panels) at various cerebral artery locations. Thick line represents the averaged waveform. Blood flow was measured with color-coded duplex ultrasound. Pressure was measured with applanation tonometry in the superficial temporal artery (*B*) and common carotid (*E* and *F*). *A*: middle cerebral artery. *C*: vertebral artery. Flow rate waveforms were not available due to poor quality measurements in one volunteer in *D*.

thus we conclude that the 1-D model may very well be used as an efficient model for predicting pressure and flow wave propagation in the entire arterial tree.

Validation of the 1-D Model

A major driver for undertaking the present study was the lack of any previous validation of the 1-D model prediction with in vivo data. 1-D models have been used for more than 30 yr to predict or analyze pressure and flow in the arterial tree, but few studies have performed a quantitative assessment of the validity of the 1-D results. Such a quantitative assessment was performed in vitro in an elastic tube network dimensioned to resemble the human arterial tree by Matthys et al. (34) . The results were supportive of the capacity of the 1-D model to

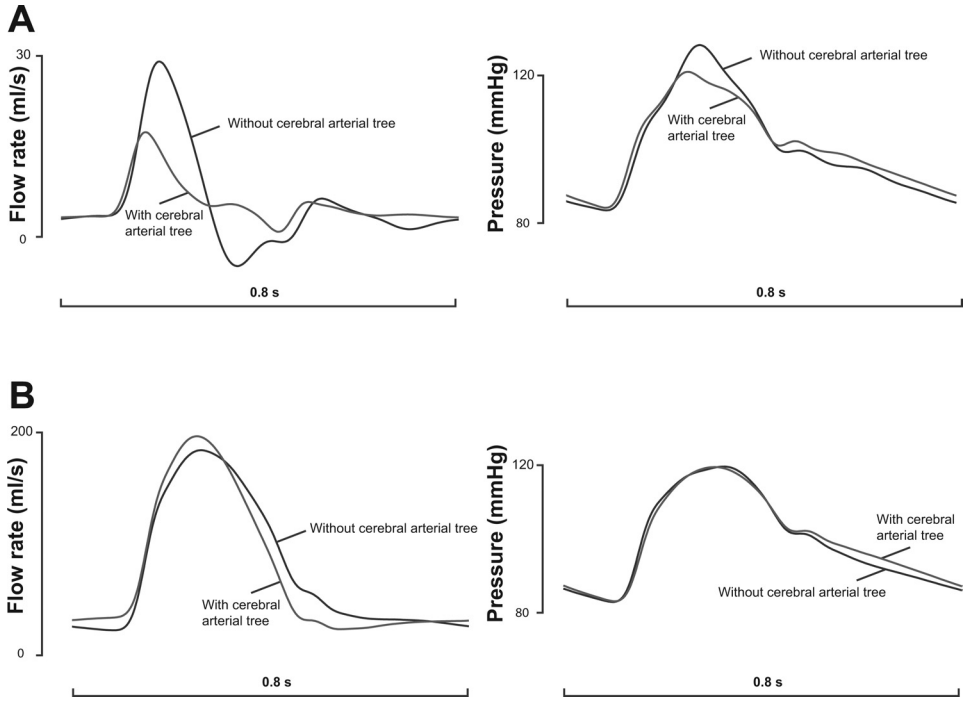

Fig. 6. Pressure and flow waveform in the common carotid (*A*) and thoracic aorta (*B*) as predicted by the present one-dimensional model containing a detailed description of the cerebral circulation as well as by the model of Stergiopulos et al. (64) containing only the major vessels feeding into the cerebral circulation.

yield good predictions; however, neither the form of the waves nor the elastic properties of the in vitro tube network were matching faithfully their physiological counterparts, so the desire to validate the 1-D model using in vivo measurements remained.

In vivo validation is a difficult task. The difficulty arises from the fact that a fully quantitative validation would require a "subject-specific" approach, where all parameters defining the 1-D model (geometry, viscoelastic properties, peripheral impedances, and varying elastance of the heart) are measured or estimated precisely on a specific subject. Only then, 1-D model predictions at several arterial locations could be compared quantitatively with the in vivo measurements in the same person and the same locations. This is clearly a formidable, if not impossible task. We therefore opted for an alternate, less quantitative but easier to implement solution: perform measurements on a group of young individuals and obtain average pressure and flow waveforms at different arterial sites, which are then compared with the 1-D model predictions. The logic behind our approach lies in that the 1-D model is constructed based on literature values reflecting, to a certain extent, the average young adult. In that respect, the general 1-D model may not reflect the characteristics of a single specific subject, but it should be, qualitatively at least, close to the average of a group of young subjects. The consequence of this approach is that the comparison can only be carried out by examining the qualitative characteristics of the pressure and flow waveforms, such as the wave shape at different arterial locations, rather than the absolute values of the pressure and flow waveform.

The qualitative comparison between the model predictions and measured pressure and flow waveforms is judged overall quite satisfactory. The results show that the model is able to reproduce the main aspects and features of physiological flow and pressure waveforms in large systemic arteries (Fig. 4) as well as in the arteries of the cerebral circulation (Fig. 5). In the aorta, model predictions have captured well the existence of a significant backflow in early diastole in the infrarenal region (Fig. 4*C*) and in the common iliac artery (Fig. 4*D*), a well-known feature that is also seen in our MRI measurements. Backflow is absent in the suprarenal aorta, a characteristic also present in the predicted flow waveforms. Comparisons are particularly interesting in the cerebral circulation, where flow waveforms are more complex and exhibit significant variations in their shape at different locations. We observe that the model captures quite well most of the qualitative wave shape features of flow in all cerebral sites. Measured flow waves in the common and internal carotid exhibit a sharp primary systolic peak followed by a second less pronounced peak in early diastole. Model predictions captured well these characteristics. Measured flow waves in the vertebral artery show a "3-peak structure," with a second shallow peak appearing in late systole. Again, model predictions show the same structure. Flow in the middle cerebral artery exhibits a characteristic plateau midway in the descending part of the systolic peak, and this feature is well represented also in the flow predicted by the model. The same plateau appears also in the temporal pressure wave measured by tonometry in vivo, and it is also present in the model predictions. There seems to be less good of an agreement in the shape of measured and predicted common carotid pressures, both shapes resembling a typical ascending aorta wave, which is expected by the proximity of the vessel to the aorta (25, 35). Radial pressure waveform presents the same sharp peak at systole between the model and in vivo measurements, which is in accordance with data reported by Kelly et al. (25) McDonald et al. (35). This feature is typical of person in the second to fourth decade and different from elderly people, where increased and faster wave reflections occur at the end of systole.

Importance of Viscoelasticity, Convective Acceleration, and Wall Friction Formulation

As seen in Table 1, very few of the previous models have introduced viscoelastic effects in their formulation. This is probably due to the fact that limited data are available on the viscoelastic properties of the human arterial wall. Yet, energy losses and damping effects due to wall viscoelasticity are of the same order magnitude as wall friction in large and medium size vessels. Table 6 shows that adding viscoelasticity leads to changes in the predicted pressure and flow in the order of a few percent in the thoracic aorta, and this is consistent with previous finding [Segers et al. (53)]. The effects become more significant in the periphery, especially on the flow wave. We may thus conclude that viscoelastic effects maybe important, especially when fine details on peripheral sites are sought. The way we have modeled viscoelasticity is not unique and the data upon which we derived the viscoelastic properties of the entire arterial tree are from the classic study of Bergel (5), performed on a limited number of canine arteries. Hence, there is clearly a need for a consistent set of data derived from human subjects.

Our model is the only global arterial tree model that includes viscoelastic effects and nonlinear wall elasticity at the same time. Avolio (2) and Fitchet et al. (13) have developed models of the entire arterial tree including viscoelastic effects but have considered a linear constitutive relation for the arterial wall. The effects of nonlinearity have not been analyzed in detail here, because this has been done in detail earlier in the work of Segers et al. (53). Segers et al. found that the root mean square of the difference of difference in pressure between a linear and nonlinear model is in the order of 2% in the aorta to 3% in the brachial artery and to almost 9% in the femoral artery. The differences are thus more significant in peripheral arteries and of the same order as the viscoelastic effects.

Wall friction and convective acceleration terms were derived from Witzig-Womersley's theory. This is, of course, still a rough approximation, because it assumes straight, rigid tubes and developed flow. Entry effects, curvature, nonplanar geometries, and bifurcations would lead to substantial deviations from Witzig-Womersley's theory, with wall shear stress being rather underestimated in most cases. Witzig-Womersley's theory, constitutes, nevertheless, an improvement over the Poiseuille flow approximation, which has often been used for estimating friction and the convective acceleration term (Table 1). We evaluated the difference it makes to use Witzig-Womersley's theory instead of simple quasi-static Poiseuille on predicted pressure and flow at different arterial locations, and the results are presented in Table 6. With the exception of pressure in the thoracic aorta, the effects of replacing Poiseuille by Witzig-Womersley's theory on both the friction term and the convective acceleration term were significant and of the same order of magnitude as the viscoelastic effects. We therefore conclude that, as for viscoelasticity, if details are sought, we should develop more precise ways of modeling the friction and convective acceleration terms. This may require developing semi-empirical models for taking into account nondeveloped flow and the effects of curvature, branching, and nonplanar geometries.

Cerebral Circulation

With the exception of models specifically designed for studying wave propagation in the cerebral circulation (1, 19, 29), most of the other earlier 1-D models included a very simplified representation of the cerebral circulation, with typically only the major proximal vessels (i.e., carotids and vertebrals) being included in the model (Table 1). We have hypothesized that the completeness of the cerebral circulation is necessary for obtaining an accurate prediction of pressure and flow not only in the distal vessels and in the vicinity of the circle of Willis but also in the proximal major vessels (i.e., carotids and vertebrals). The rational for this hypothesis is that the distal cerebral arterial tree constitutes a complex arterial network with specific topological wave transmission and reflection properties, which will influence considerable pressure and flow in the entire cerebral circulation. The importance of a detailed cerebral arterial tree on wave reflections was first recognized by Avolio (2). Our results indeed show that predicted wave shapes in the carotid artery are strongly affected by the presence of a detailed model of the distal cerebral circulation. This was clearly demonstrated in Fig. 6, where the shape of the predicted common carotid pressure and flow is substantially different when the detailed cerebral arterial tree (Fig. 2*D*) is substituted by the simplistic one of Stergiopulos et al. (Fig. 2*A*; Ref. 64). The effects on the flow waveform are remarkable, despite the fact that the distal impedances at the termination points of the simple cerebral arterial tree model were carefully set to match the resistive and compliant characteristics of the detailed cerebral tree. Of particular importance is the enhanced pulsation, which exhibits the flow wave in absence of the detailed distal cerebral tree. The enhanced pulsation leads to negative flow in early diastole, a phenomenon clearly nonphysiological, because we know from in vivo measurements that flow is purely unidirectional in the carotid.

Table 6. *Effect of viscoelasticity, wall shear stress, and convective acceleration formulation on pressure and flow rate waveforms for 3 representative arterial sites*

Viscoelasticity	Wall Shear Stress*	Convective Acceleration*	Thoracic Aorta		Common Iliac Artery		Middle Cerebral Artery	
			Pressure, mmHg	Flow rate, ml/s	Pressure, mmHg	Flow rate, ml/s	Pressure, mmHg	Flow rate, ml/s
+	−	−	1.5 (1.5%)	4.0 (4.3%)	2.3 (2.4%)	1.4 (15%)	2.3 (2.4%)	0.09 (4.5%)
−	+	−	0.4 (0.4%)	4.0 (4.3%)	2.0 (2.1%)	1.5 (16%)	2.0 (2.1%)	0.09 (4.5%)
−	−	+	1.3 (1.3%)	11.3 (12%)	6.3 (6.6%)	4.4 (4.6%)	2.1 (2.2%)	0.07 (3.5%)
+	+	+	2.5 (2.5%)	11.1 (12%)	6.8 (7.2%)	4.8 (5.1%)	3.7 (3.9%)	0.11 (5.5%)

Values are the root mean square of the difference over the entire pressure or flow wave in absolute (relative to the reference model in %). Reported data are difference between a "control" model using varying elastance model but not considering viscoelasticity, improved wall shear stress, and convective acceleration terms and models that consecutively consider viscoelasticity, wall shear stress, and convective acceleration formulation. *Improved wall shear stress and convective acceleration terms from Witzig-Womersley theory.

We attribute these effects to the enhanced, nonphysiological wave reflection properties of the simplified cerebral tree, and in that respect we agree with Avolio (2). We therefore conclude that a detailed cerebral arterial tree is necessary for obtaining accurate pressure and flows in the cerebral circulation, even in the major proximal cerebral vessels. On the other hand, the effects of the cerebral circulation in the aorta are, as expected, minimal (Fig. 6*B*). This means that if the scope of the model is confined in all the other vessels of the systemic circulation and not concerned with cerebral blood flow, a detailed description of the cerebral circulation may not be necessary. We note, however, that abnormally high reflection coefficients in the main systemic arteries, such as those present in the original Noordergraaf-Westerhof model, lead to nonphysiological waves along the aorta, manifested by the presence of excessive reflected waves and high augmentation index in the ascending aorta. The optimization of all reflection sites performed in the present model improved the wave reflection profile and led to physiological pressure waves in the aorta.

Heart Model

Most of the previous 1-D models of the arterial circulation used as proximal boundary conditions a prescribed pressure or flow wave. This is of course acceptable; however, it implies that the chosen proximal wave corresponds to the particular state of the arterial tree. This is because the aortic pressure and flow wave are the results of the interaction of the heart and the arterial system, and therefore any change in either the cardiac parameters (i.e., heart rate, contractility, filling, etc.) or the arterial parameters (i.e., resistance, compliance, etc.) would lead to changes in the aortic pressure and flow. Hence, the approach to describe pressure or flow as a proximal boundary condition is very limiting, especially for performing parametric studies involving changes in the cardiac side, the arterial side or both. Using a heart model, as the varying elastance model employed here, allows for such flexibility. The resulting pressure and flow waves are physiological and compare well, as seen in Figs. 4 and 5, with the measured waves. Although not in the scope of the present study and thus not presented in this work, we performed a number of parametric studies, where we varied cardiac and arterial parameters and we obtained reasonable pressure and flow predictions, reinforcing thus the general applicability of the heart model. Additional studies are required to further validate the heart-arterial system interaction process as captured by our 1-D model.

Limitations and Future Work

Limitations of the model with respect to the formulations of viscoelasticity, wall friction, and convective acceleration terms have been discussed above. The heart model is also a simplistic one, and there is evidence that the varying elastance curve may not be invariable with disease (24). The model neglects venous circulation as well as pulmonary circulation. The effects of CSF circulation surrounding intracranial arteries have not been taken into account. The limitations of the windkessel models employed in the cerebral circulation are not known and need to be investigated in detail. Autoregulation phenomena, playing an important role in the cerebral and coronary circulation, are neglected. The coronary tree model is also a simplistic one, requiring further modeling efforts to include the effects of myocardial contraction on vessels and peripheral coronary beds.

The validation has been restricted to a group of young volunteers. Future work will consider the effects of aging and disease on arterial wall properties, peripheral impedances, and cardiac function, and validation on aged subjects or patients group will be performed.

This work permitted us to qualitatively validate the predictions of a generic arterial tree model based on averaged in vivo measurements on volunteers. Future work will be focused on a quantitative validation of the model on a specific subject. The arterial tree will be constructed based on geometry and elasticity data derived from measurements on the specific person, and model predictions will be compared with noninvasive in vivo measurements on the same subject.

Conclusions

We have extended and improved a previous 1-D model of the systemic circulation by including a heart model, a detailed description of the cerebral arterial tree, viscoelasticity, and a Witzig-Womersley theory-based formulation for the friction and convective acceleration terms. The model predicts pressure and flow waves which are in fairly good qualitative agreement with in vivo measurements, especially with respect to the shape and wave details. The results obtained validate the model predictions of pressure and flow in central arteries as well as in major arteries of the brain, reinforcing thus the general applicability of the model to the entire systemic and cerebral circulation.

ACKNOWLEDGMENTS

We thank François Lazeyras and Pascal Challande from the Center for Biomedical Imaging at the University Hospital of Geneva for the MRI measurements and Virginie Chenaux for the work performed during a Ecole Polytechnique Fédérale de Lausanne master thesis project.

GRANTS

This work was supported by the European Commission Contract No. IST-027703 @neurIST Project. The MRI research was funded by the Center for Biomedical Imaging at the University Hospital of Geneva and Ecole Polytechnique Fédérale de Lausanne.

REFERENCES

1. **Alastruey J, Parker KH, Peiro J, Byrd SM, Sherwin SJ.** Modelling the circle of Willis to assess the effects of anatomical variations and occlusions on cerebral flows. *J Biomech* 40: 1794–1805, 2007.
2. **Avolio AP.** Multi-branched model of the human arterial system. *Med Biol Eng Comput* 18: 709–718, 1980.
3. **Azer K, Peskin CS.** A one-dimensional model of blood flow in arteries with friction and convection based on the womersley velocity profile. *Cardiovasc Eng* 2007 June 14 [Epub ahead of print].
4. **Baguet JP, Kingwell BA, Dart AL, Shaw J, Ferrier KE, Jennings GL.** Analysis of the regional pulse wave velocity by Doppler: methodology and reproducibility. *J Hum Hypertens* 17: 407–412, 2003.
5. **Bergel DH.** The dynamic elastic properties of the arterial wall. *J Physiol* 156: 458–469, 1961.
6. **Bessems D, Rutten M, Van De Vosse F.** A wave propagation model of blood flow in large vessels using an approximate velocity profile function. *J Fluid Mech* 580: 145–168, 2007.
7. **Buijs PC, Krabbe-Hartkamp MJ, Bakker CJ, de Lange EE, Ramos LM, Breteler MM, Mali WP.** Effect of age on cerebral blood flow: measurement with ungated two-dimensional phase-contrast MR angiography in 250 adults. *Radiology* 209: 667–674, 1998.
8. **Campbell KB, Ringo JA, Wakao Y, Klavano PA, Alexander JE.** Internal capacitance and resistance allow prediction of right ventricle outflow. *Am J Physiol Heart Circ Physiol* 243: H99–H112, 1982.

9. **Cassot F, Vergeur V, Bossuet P, Hillen B, Zagzoule M, Marc-Vergnes JP.** Effects of anterior communicating artery diameter on cerebral hemodynamics in internal carotid artery disease: a model study. *Circulation* 92: 3122–3131, 1995.
10. **Cassot F, Zagzoule M.** and Marc-Vergnes J.P Hemodynamic role of the circle of Willis in stenoses of internal carotid arteries An analytical solution of a linear model. *J Biomech* 33: 395–405, 2000.
11. **Dodge JT Jr, Brown BG, Bolson EL, Dodge HT.** Lumen diameter of normal human coronary arteries Influence of age, sex, anatomic variation, and left ventricular hypertrophy or dilation. *Circulation* 86: 232–246, 1992.
12. **Enzmann DR, Ross MR, Marks MP, Pelc NJ.** Blood flow in major cerebral arteries measured by phase-contrast cine MR. *Am J Neuroradiol* 15: 123–129, 1994.
13. **Fitchett DH.** LV-arterial coupling: interactive model to predict effect of wave reflections on LV energetics. *Am J Physiol Heart Circ Physiol* 261: H1026–H1033, 1991.
14. **Formaggia L, Lamponi D, Tuveri M, Veneziani A.** Numerical modeling of 1D arterial networks coupled with a lumped parameters description of the heart. *Comput Methods Biomech Biomed Engin* 9: 273–288, 2006.
15. **Fox C, Davies MJ, Webb-Peploe MM.** Length of left main coronary artery. *Br Heart J* 35: 796–798, 1973.
16. **Gabrielsen TO, Greitz T.** Normal size of the internal carotid, middle cerebral and anterior cerebral arteries. *Acta Radiol* 10: 1–10, 1970.
17. **Giller CA, Aaslid R.** Estimates of pulse wave velocity and measurement of pulse transit time in the human cerebral circulation. *Ultraschall Med Biol* 20: 101–105, 1994.
18. **Hayashi K, Nagasawa S, Naruo Y, Okumura A, Moritake K, Handa H.** Mechanical properties of human cerebral arteries. *Biorheology* 17: 211–218, 1980.
19. **Hillen B, Hoogstraten HW, Post L.** A mathematical model of the flow in the circle of Willis. *J Biomech* 19: 187–194, 1986.
20. **Holdsworth DW, Norley CJ, Frayne R, Steinman DA, Rutt BK.** Characterization of common carotid artery blood-flow waveforms in normal human subjects. *Physiol Meas* 20: 219–240, 1999.
21. **Holenstein R, Niederer P, Anliker M.** A viscoelastic model for use in predicting arterial pulse waves. *J Biomech Eng* 102: 318–325, 1980.
22. **Huo Y, Kassab GS.** A hybrid one-dimensional/Womersley model of pulsatile blood flow in the entire coronary arterial tree. *Am J Physiol Heart Circ Physiol* 292: H2623–H2633, 2007.
23. **Ioannou CV, Stergiopulos N, Katsamouris AN, Startchik I, Kalangos A, Licker MJ, Westerhof N, Morel DR.** Hemodynamics induced after acute reduction of proximal thoracic aorta compliance. *Eur J Vasc Endovasc Surg* 26: 195–204, 2003.
24. **Jegger D, Mallik AS, Nasratullah M, Jeanrenaud X, da Silva R, Tevaearai H, von Segesser LK, Stergiopulos N.** The effect of a myocardial infarction on the normalized time-varying elastance curve. *J Appl Physiol* 102: 1123–1129, 2007.
25. **Kelly R, Hayward C, Avolio A, O'Rourke M.** Noninvasive determination of age-related changes in the human arterial pulse. *Circulation* 80: 1652–1659, 1989.
26. **Krabbe-Hartkamp MJ, van der Grond J, de Leeuw FE, de Groot JC, Algra A, Hillen B, Breteler MM, Mali WP.** Circle of Willis: morphologic variation on three-dimensional time-of-flight MR angiograms. *Radiology* 207: 103–111, 1998.
27. **Krams R, Sipkema P, Westerhof N.** Varying elastance concept may explain coronary systolic flow impediment. *Am J Physiol Heart Circ Physiol* 257: H1471–H1479, 1989.
28. **Krayenbuehl H, Yasargil MG.** *Cerebral Angiography*. New York: Thieme Medical, 1982.
29. **Kufahl RH, Clark ME.** A circle of Willis simulation using distensible vessels and pulsatile flow. *J Biomech Eng* 107: 112–122, 1985.
30. **Langewouters GJ.** *Visco-Elasticity Of The Human Aorta In Vitro In Relation To Pressure And Age*. 1982, p. 221.
31. **Latham RD, Westerhof N, Sipkema P, Rubal BJ, Reuderink P, Murgo JP.** Regional wave travel and reflections along the human aorta: a study with six simultaneous micromanometric pressures. *Circulation* 72: 1257–1269, 1985.
32. **Luchsinger PC, Snell RE, Patel DJ, Fry DL.** Instanteous pressure distribution along the human aorta. *Circ Res* 15: 503–510, 1964.
33. **Marshall I, Papathanasopoulou P, Wartolowska K.** Carotid flow rates and flow division at the bifurcation in healthy volunteers. *Physiol Meas* 25: 691–697, 2004.
34. **Matthys KS, Alastruey J, Peiro J, Khir AW, Segers P, Verdonck PR, Parker KH, Sherwin SJ.** Pulse wave propagation in a model human arterial network: assessment of 1-D numerical simulations against in vitro measurements. *J Biomech* 40: 3476–3486, 2007.
35. **McDonald DA, Nichols WW, O'Rourke MF.** *Blood Flow in Arteries*. London: Edward Arnold, 1990.
36. **Meister JJ.** Mesure par échographie Doppler et modélisation théorique de l'effet de troubles cardiaques sur la pression et le débit artériels (PhD thesis). *Lausanne* 4: 125, 1983.
37. **Merenda F.** *Varying Elastance Model Coupled to a Distributed Model of the Human Arterial Tree.* Lausanne, Switzerland: Ecole Polytechnique Fédérale de Lausanne, 2003.
38. **Murgo JP, Westerhof N, Giolma JP, Altobelli SA.** Aortic input impedance in normal man: relationship to pressure wave forms. *Circulation* 62: 105–116, 1980.
39. **Nichols WW, O'Rourke MF, Avolio AP, Yaginuma T, Murgo JP, Pepine CJ, Conti CR.** Effects of age on ventricular-vascular coupling. *Am J Cardiol* 55: 1179–1184, 1985.
40. **Noordergraaf A.** *Physical Basis of Ballistocardiography*. s'Gravenhage, The Netherlands: Excelsior, 1956, p. 146.
41. **Noordergraaf A, Verdouw D, Boom HB.** The use of an analog computer in a circulation model. *Prog Cardiovasc Dis* 5: 419–439, 1963.
42. **Obata T, Shishido F, Koga M, Ikehira H, Kimura F, Yoshida K.** Three-vessel study of cerebral blood flow using phase-contrast magnetic resonance imaging: effect of physical characteristics. *Magn Reson Imaging* 14: 1143–1148, 1996.
43. **Olufsen MS.** Structured tree outflow condition for blood flow in larger systemic arteries. *Am J Physiol Heart Circ Physiol* 276: H257–H268, 1999.
44. **Olufsen MS, Peskin CS, Kim WY, Pedersen EM, Nadim A, Larsen J.** Numerical simulation and experimental validation of blood flow in arteries with structured-tree outflow conditions. *Ann Biomed Eng* 28: 1281–1299, 2000.
45. **Papageorgiou GL, Jones BN, Redding VJ, Hudson N.** The areas ratio of normal arterial junctions and its implications in pulse wave reflections. *Cardiovasc Res* 24: 478–484, 1990.
46. **Papapanayotou CJ, Cherruault Y, Delarochefoucauld B.** A mathematical-model of the circle of Willis in the presence of an arteriovenous anomaly. *Comput Math Appl* 20: 199–206, 1990.
47. **Pennell DJ, Keegan J, Firmin DN, Gatehouse PD, Underwood SR, Longmore DB.** Magnetic resonance imaging of coronary arteries: technique and preliminary results. *Br Heart J* 70: 315–326, 1993.
48. **Raines JK, Jaffrin MY, Shapiro AH.** A computer simulation of arterial dynamics in the human leg. *J Biomech* 7: 77–91, 1974.
49. **Sagawa K.** *Cardiac Contraction and the Pressure-Volume Relationship*. Oxford, UK: Oxford University Press, 1988, p. 15.
50. **Schaaf BW, Abbrecht PH.** Digital computer simulation of human systemic arterial pulse wave transmission: a nonlinear model. *J Biomech* 5: 345–364, 1972.
51. **Scheel P, Ruge C, Petruch UR, Schoning M.** Color duplex measurement of cerebral blood flow volume in healthy adults. Stroke; a journal of cerebral. *Circulation* 31: 147–150, 2000.
52. **Segers P, Rietzschel E, Heireman S, De Buyzere M, Gillebert T, Verdonck P, Van Bortel L.** Carotid tonometry versus synthesized aorta pressure waves for the estimation of central systolic blood pressure and augmentation index. *Am J Hypertens* 18: 1168–1173, 2005.
53. **Segers P, Stergiopulos N, Verdonck P, Verhoeven R.** Assessment of distributed arterial network models. *Med Biol Eng Comput* 35: 729–736, 1997.
54. **Senzaki H, Chen CH, Kass DA.** Single-beat estimation of end-systolic pressure-volume relation in humans. *A* new method with the potential for noninvasive application. *Circulation* 94: 2497–2506, 1996.
55. **Sherwin SJ, Franke V, Peiro J, Parker K.** One-dimensional modelling of a vascular network in space-time variables. *J Engin Math* 47: 217–250, 2003.
56. **Shroff SG, Janicki JS, Weber KT.** Evidence and quantitation of left ventricular systolic resistance. *Am J Physiol Heart Circ Physiol* 249: H358–H370, 1985.
57. **Spilt A, Box FM, van der Geest RJ, Reiber JH, Kunz P, Kamper AM, Blauw GJ, van Buchem MA.** Reproducibility of total cerebral blood flow measurements using phase contrast magnetic resonance imaging. *J Magn Reson Imaging* 16: 1–5, 2002.
58. **Starling MR, Walsh RA, Dell'Italia LJ, Mancini GB, Lasher JC, Lancaster JL.** The relationship of various measures of end-systole to left

ventricular maximum time-varying elastance in man. *Circulation* 76: 32–43, 1987.
59. **Stergiopulos N, Meister JJ, Westerhof N.** Evaluation of methods for estimation of total arterial compliance. *Am J Physiol Heart Circ Physiol* 268: H1540–H1548, 1995.
60. **Stergiopulos N, Meister JJ, Westerhof N.** Scatter in input impedance spectrum may result from the elastic nonlinearity of the arterial wall. *Am J Physiol Heart Circ Physiol* 269: H1490–H1495, 1995.
61. **Stergiopulos N, Meister JJ, Westerhof N.** Simple and accurate way for estimating total and segmental arterial compliance: the pulse pressure method. *Ann Biomed Eng* 22: 392–397, 1994.
62. **Stergiopulos N, Segers P, Westerhof N.** Use of pulse pressure method for estimating total arterial compliance in vivo. *Am J Physiol Heart Circ Physiol* 276: H424–H428, 1999.
63. **Stergiopulos N, Westerhof BE, Westerhof N.** Physical basis of pressure transfer from periphery to aorta: a model-based study. *Am J Physiol Heart Circ Physiol* 274: H1386–H1392, 1998.
64. **Stergiopulos N, Young DF, Rogge TR.** Computer simulation of arterial flow with applications to arterial and aortic stenoses. *J Biomech* 25: 1477–1488, 1992.
65. **Stettler JC, Niederer P, Anliker M.** Theoretical analysis of arterial hemodynamics including the influence of bifurcations. Part I: mathematical models and prediction of normal pulse patterns. *Ann Biomed Eng* 9: 145–164, 1981.
66. **Stettler JC, Niederer P, Anliker M, Casty M.** Theoretical analysis of arterial hemodynamics including the influence of bifurcations. Part II: critical evaluation of theoretical model and comparison with noninvasive measurements of flow patterns in normal and pathological cases. *Ann Biomed Eng* 9: 165–175, 1981.
67. **Stock KW, Wetzel SG, Lyrer PA, Radu EW.** Quantification of blood flow in the middle cerebral artery with phase-contrast MR imaging. *Eur Radiol* 10: 1795–1800, 2000.
68. **Vis MA, Sipkema P, Westerhof N.** Modeling pressure-area relations of coronary blood vessels embedded in cardiac muscle in diastole and systole. *Am J Physiol Heart Circ Physiol* 268: H2531–H2543, 1995.
69. **Wan J, Steele B, Spicer SA, Strohband S, Feijoo GR, Hughes TJ, Taylor CA.** A one-dimensional finite element method for simulation-based medical planning for cardiovascular disease. *Comput Methods Biomech Biomed Engin* 5: 195–206, 2002.
70. **Wemple RR, Mockros LF.** Pressure and flow in the systemic arterial system. *J Biomech* 5: 629–641, 1972.
71. **Westerhof N, Bosman F, De Vries CJ, Noordergraaf A.** Analog studies of the human systemic arterial tree. *J Biomech* 2: 121–143, 1969.
72. **Westerhof N, Stergiopulos N.** Models of the arterial tree. *Stud Health Technol Inform* 71: 65–77, 2000.
73. **Yasargil MG.** *Microneurosurgery: Microsurgical Anatomy of the Basal Cisterns and Vessels of the Brain, Diagnostic Studies, General Operative Techniques and Pathological Considerations of the Intracranial Aneurysms.* New York: Thieme Medical, 1984.
74. **Zagzoule M, Marc-Vergnes JP.** A global mathematical model of the cerebral circulation in man. *J Biomech* 19: 1015–1022, 1986.